

## Supplementary Information

### **Tunable product selectivity on demand: Mechanism-guided Lewis acid co-catalyst for CO<sub>2</sub> electroreduction to ethylene glycol**

Yifei Li<sup>1</sup>, Karin Calvinho<sup>1,3</sup>, Mahak Dhiman<sup>1</sup>, Anders Laursen<sup>1,3</sup>, Hengfei Gu<sup>1</sup>, Dominick Santorelli<sup>1</sup>, Zachary Clifford<sup>1</sup>, G. Charles Dismukes<sup>1,2\*</sup>

<sup>1</sup>*Department of Chemistry and Chemical Biology, Rutgers, The State University of New Jersey, 123 Bevier Road, Piscataway, New Jersey, 08854*

<sup>2</sup>*Waksman Institute, Rutgers, The State University of New Jersey, 190 Frelinghuysen Road, Piscataway, New Jersey, 08854*

<sup>3</sup>*Renew CO<sub>2</sub> Inc. 418 Orchard Street Cranford, NJ 07016-1745,*

\*Corresponding author ([dismukes@rutgers.edu](mailto:dismukes@rutgers.edu))

## 1. Scanning Electron Microscopy

The nickel phosphides were characterized by a Zeiss Sigma Field Emission SEM in-lens detector supported on conductive carbon. SEM images of as-synthesized  $\text{Ni}_2\text{P}$  loose powders (top row) showing polydisperse particles. The bottom row of images shows the morphology of the  $\text{Ni}_2\text{P}$  catalyst pellets after at least three  $\text{CO}_2\text{RR}$  turnovers. As shown in the EDS mapping, the distribution of Ni and P is uniform when examining flat surfaces. On regions with lower depth, the P signal drops off compared to the Ni signal, due to the higher atomic number of Ni compared to P causing different focusing from the non-flat nature of agglomerates. As shown in Fig. S1c, the particles have diameters ranging from 2 to 16 micrometers with mean size of 6 micrometers.

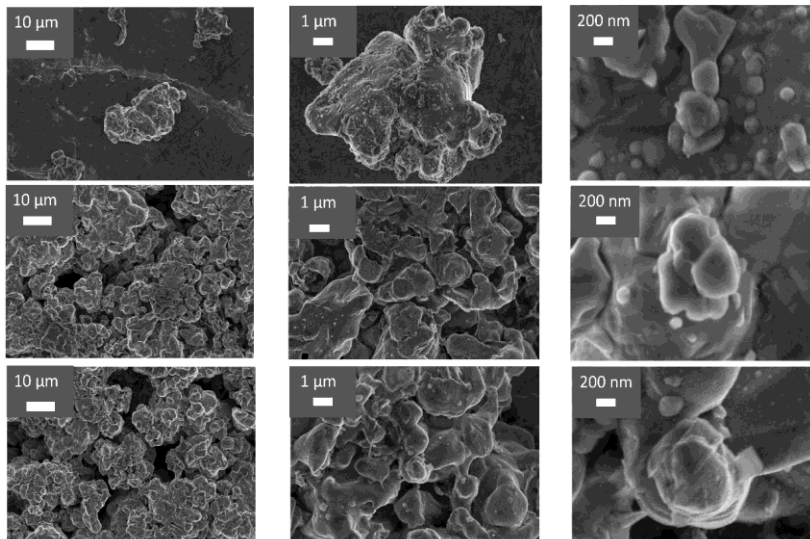


*Fig. S1a: SEM images of an as-synthesized  $\text{Ni}_2\text{P}$  polycrystalline powder (top row). The cathode ( $\text{Ni}_2\text{P}$  + Nafion pressed pellet) before electrolysis (middle row). The cathode ( $\text{Ni}_2\text{P}$  + Nafion pressed pellet) after electrolysis under 0 V vs RHE in 0.5 M  $\text{KHCO}_3$  and 10 mM  $\text{H}_3\text{BO}_3$  for 18 hours (bottom row).*

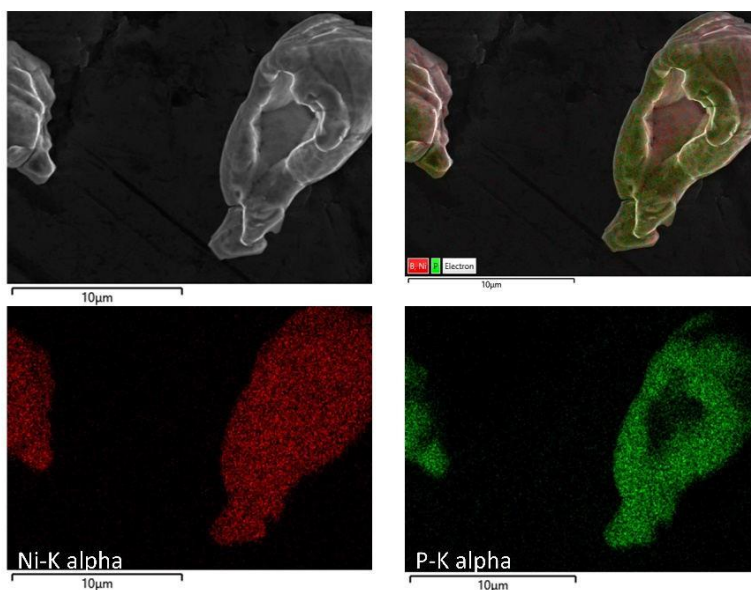


*Fig. S1b: SEM mapping of elemental distribution for as-synthesized  $\text{Ni}_2\text{P}$ .*

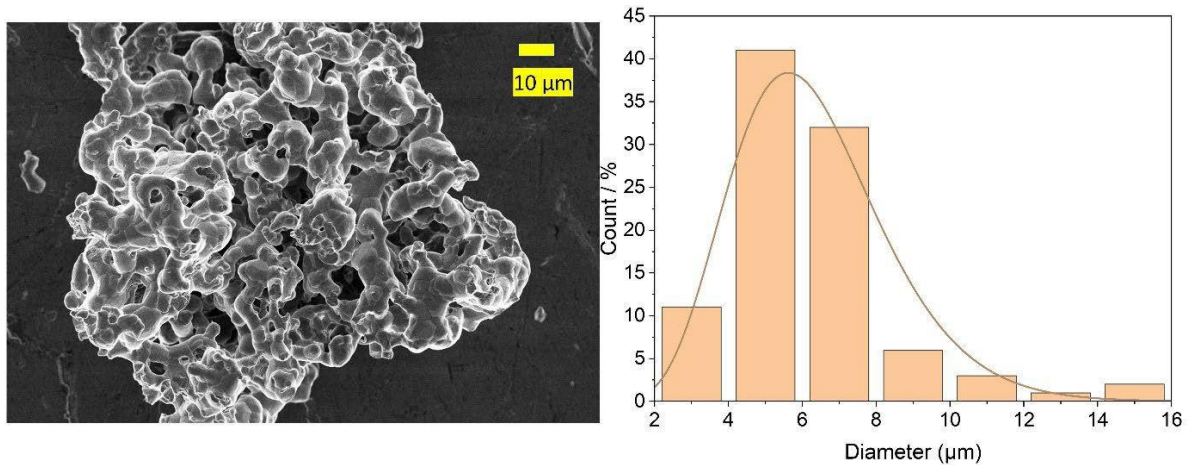


Fig. S1c: SEM particle size distribution analysis for as-synthesized  $\text{Ni}_2\text{P}$ .

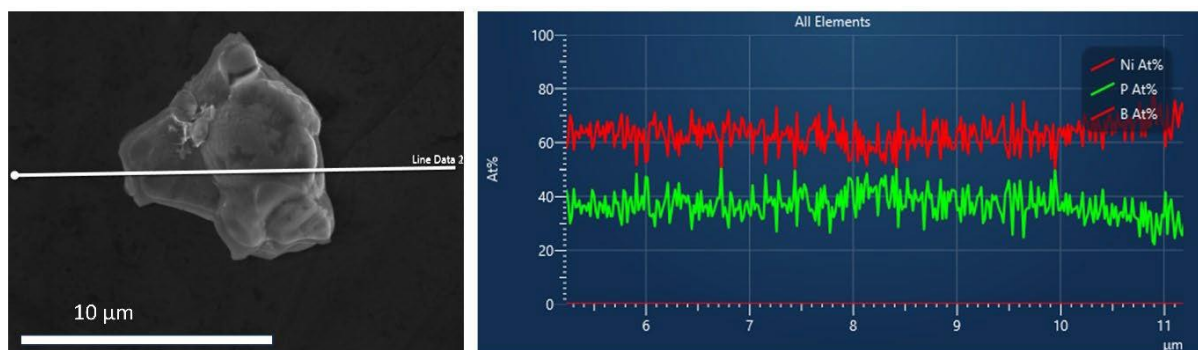


Fig. S1d: Line scan for one representative particle for as-synthesized  $\text{Ni}_2\text{P}$  and its atomic %.

## 2. Powder X-Ray Diffraction

Powder X-Ray diffraction was conducted at room temperature on a Philips Xpert system, spinning at 100 rpm, in a Bragg-Brentano geometry, using Cu K-alpha 0.15418 nm x-rays, calibrated with a Si standard. The sample holder was 3 mm deep and 1/2" in diameter, filled with the tested powder. No change of phase is observed before and after electrolysis. The diffraction pattern matches the reference without observable impurity. As shown in Fig. S2, after electrolysis, the peaks became broader which is very common and occurs when the sample contains more moisture or becomes more disordered. There is a minor shift to the right compared with the pristine electrode. This can be explained by a zero-point shift for legitimate reasons caused by errors such as sample height alignment.<sup>1</sup>

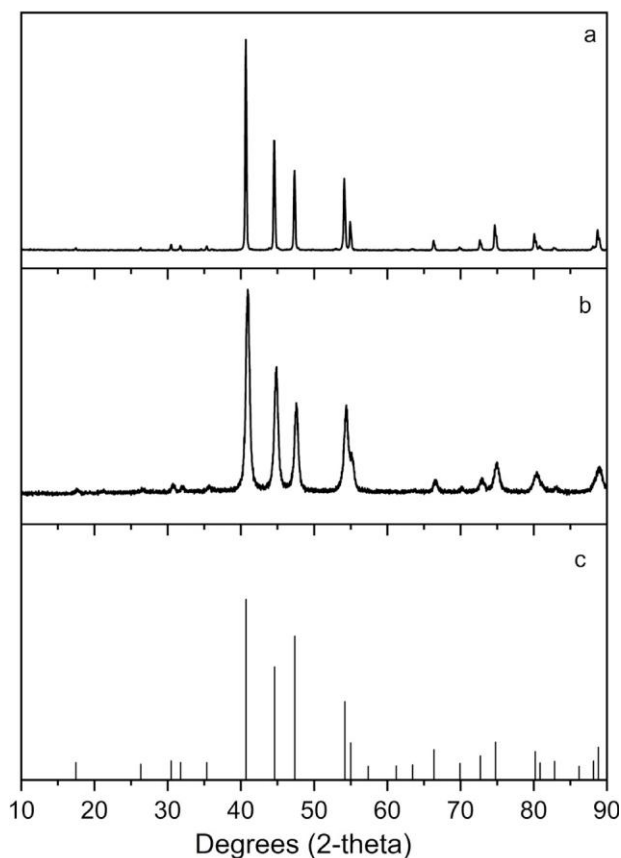


Fig. S2. Powder X-ray diffraction of as-synthesized polycrystalline Ni<sub>2</sub>P (a), Ni<sub>2</sub>P after electrolysis at 0V vs RHE in 0.5M KHCO<sub>3</sub> and 10mM H<sub>3</sub>BO<sub>3</sub> for 16 hours, and the reference pattern 01-074-1384 for Ni<sub>2</sub>P from the ICDD(c).

### 3. X-ray Photoelectron Spectroscopy

K-Alpha XPS system was used with 180° double-focusing hemispherical analyzer, 128-channel detector and a mono-chromated, micro-focused, low-power Al K-Alpha X-ray source.

Table S1. Peak assignments and references for deconvolution of XPS spectra.

Element	Chemical state	Peak (eV)	Reference- Binding Energy (eV)
Ni 2p	Ni(OH) <sub>2</sub>	856.0	856.1;855;856 <sup>2</sup>
	Ni <sub>2</sub> P	853.3	853.1 <sup>2</sup>
	Ni <sub>3</sub> (PO <sub>4</sub> ) <sub>2</sub>	857.8	856.6 <sup>3</sup> 859.8 <sup>4</sup>
	NiBO <sub>3</sub>	858.8	
P 2p	P-Ni <sub>2</sub> P	129.8	129.4 <sup>2</sup>
	P-Ni <sub>3</sub> (PO <sub>4</sub> ) <sub>2</sub>	133.0	133.3 <sup>2</sup>
P2s	P-Ni <sub>2</sub> P	187.4	Ni <sub>3</sub> P: 187.2 <sup>5</sup>
	P-Ni <sub>3</sub> (PO <sub>4</sub> ) <sub>2</sub>	190.7	190.7 <sup>2</sup>
B 1s	NiBO <sub>3</sub>	192.3	NiB: 188.9 <sup>2</sup> Ni <sub>2</sub> B: 189.9 <sup>2</sup> Ni <sub>3</sub> B: 187.4 <sup>2</sup> H <sub>3</sub> BO <sub>3</sub> : 193;192.8;193.6 <sup>2</sup> BPO <sub>4</sub> : 193.5 <sup>2</sup> FeBO <sub>3</sub> : 192 <sup>2</sup> CrBO <sub>3</sub> : 192.7 <sup>2</sup>

Table S2. Peak area and atomic percentage for XPS spectra

	pristine electrode		Atomic Percentage (%) for electrode after electrolysis at 10 mM H <sub>3</sub> BO <sub>3</sub>		Atomic Percentage (%) for electrode after electrolysis at 50 mM H <sub>3</sub> BO <sub>3</sub>	
	B. E. (eV)	Atomic Percentage (%)	B. E. (eV)	Atomic Percentage (%)	B. E. (eV)	Atomic Percentage (%)
Ni 2p	853.22	1.27	855.86	5.65	855.29	0.99
Ni 2p	855.95	4.51	853.57	1.95	852.82	0.57
Ni 2p	857.85	2.3	857.97	1.91	857.12	0.8
Ni 2p	860.23	1.84	860.36	1.97	862.18	0.75
Ni 2p	862.17	1.9	862.09	1.97	860.38	0.83
Ni 2p	864.17	1.14	864.15	1.19	866.24	0.23
Ni 2p					858.78	0.38
Ni 2p					864.05	0.58
P 2p	132.99	7.89	129.9	1.69	133.44	0.95
P 2p	129.81	1.41	132.86	2.99	129.89	0.37
P 2s	190.64	7.83	190.63	3.02	190.25	0.7
P 2s	187.49	1.46	187.68	2.01	187.36	0.51
B 1s					192.21	2.28
C 1s	284.6	19.03	284.75	23.32	292.17	26.61
C 1s	288.36	2.94	288.49	5.69	285.01	17.07
C 1s	291.7	1.29	292.7	4.48	295.72	9.41
C 1s	286.23	3.38	295.72	1.71	287.1	3.47
C 1s			286.46	2.23	289.31	4.88

C 1s					293.46	11.34
O 1s	531.28	34.98	531.26	34.52	531.09	10.49
O 1s	532.98	6.79	532.95	3.68	532.67	5.06
O 1s					535.35	1.71

#### 4. Determination of Uncompensated Resistance

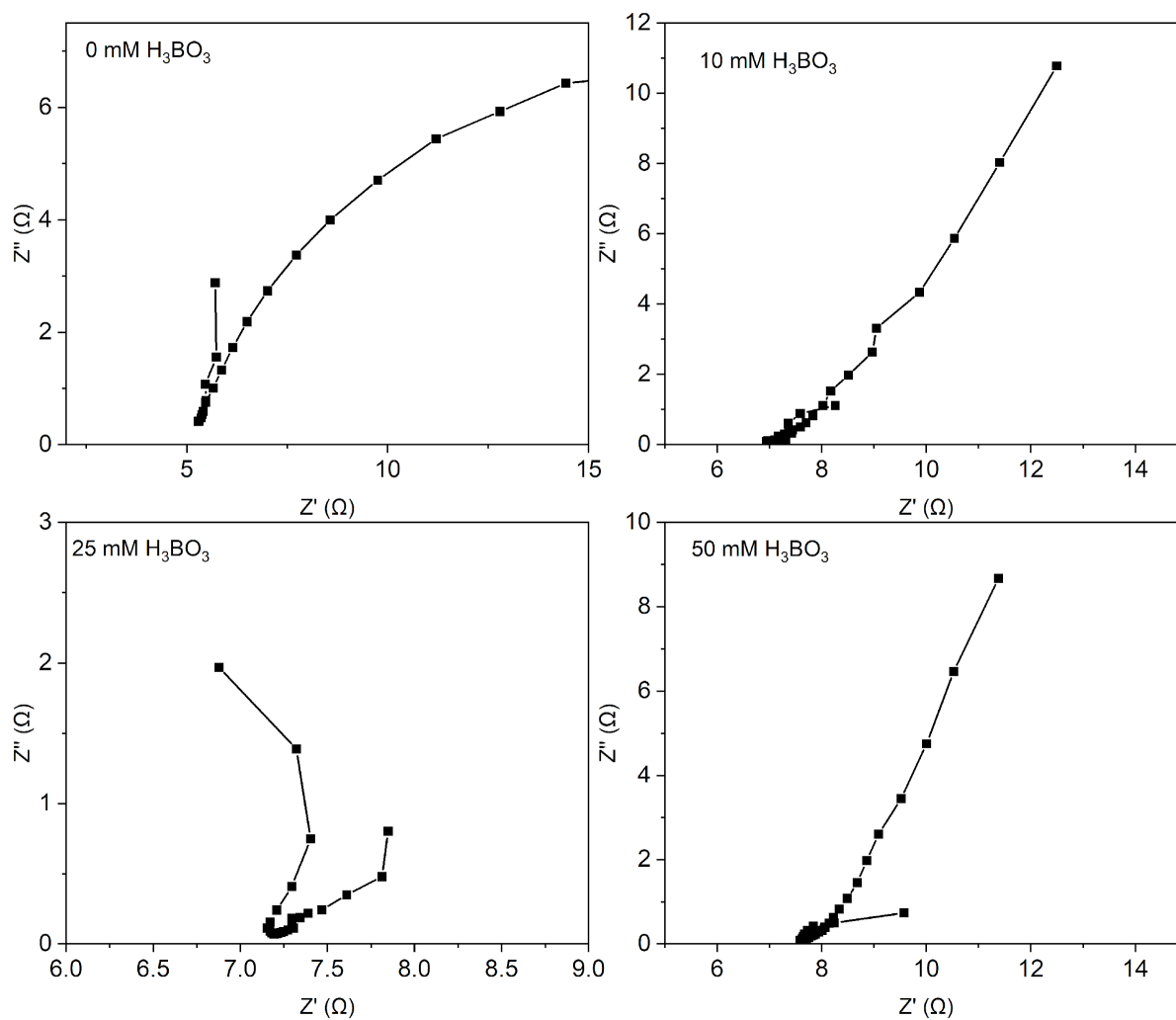


Fig. S3: Representative potentiostatic electrochemical impedance measurements of  $\text{Ni}_2\text{P}$  at 0 V vs RHE in 0.5 M  $\text{KHCO}_3$  with different concentrations of boric acid give a solution resistance of 5.0-8.0  $\Omega$ .

## 5. Analysis by $^1\text{H}$ NMR and $^{11}\text{B}$ NMR

$^1\text{H}$  NMR spectra was recorded using a Bruker Avance Neo 500MHz NMR spectrometer equipped with a RT-DR-BF/1H-5mm-Z-SP iProbe. 150  $\mu\text{L}$  samples from the  $\text{CO}_2$  reduction electrolyte after the reaction from the working electrode compartment were mixed with 100  $\mu\text{L}$  of  $\text{D}_2\text{O}$ , with the addition of 1mM  $\text{D}_2\text{O}$  as external standard.

The assignment of peaks to  $\text{HCOOH}$ , 2,3-furandiol, and methylglyoxal was done according to Calvinho. et al which used chemical standards<sup>6</sup>.

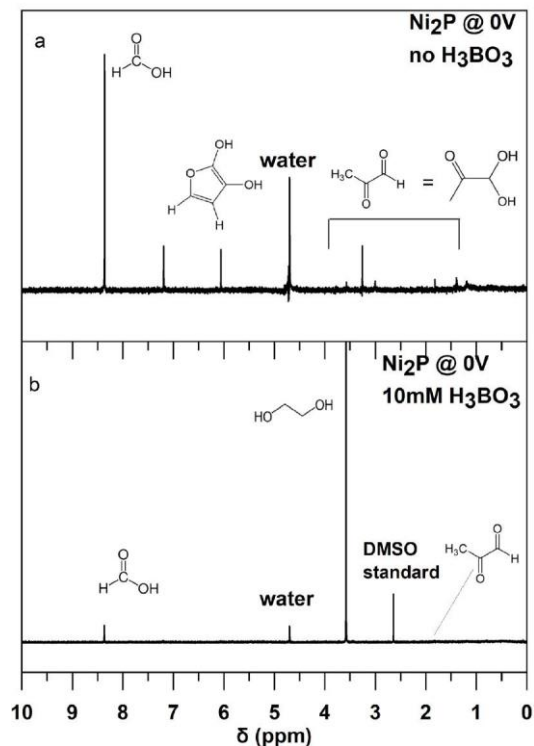


Fig. S4: (a)  $^1\text{H}$  NMR of a catholyte sample from the electroreduction of  $\text{CO}_2$  on  $\text{Ni}_2\text{P}$  in  $0.5\text{M KHCO}_3$  at  $0\text{V}$  vs RHE; (b) Same conditions in  $0.5\text{M KHCO}_3$  plus  $10\text{mM}$  boric acid.

Table S3a.  $^1\text{H}$  NMR shifts for  $\text{CO}_2\text{RR}$  products and references.

	Chemical Shifts (ppm)	Reference (ppm)
formic acid	8.4 (s)	8.4 (s) <sup>6</sup>
2,3- furandiol	7.2 (s); 6.1 (s)	7.2 (s); 6.1 (s) <sup>6</sup>
Methylglyoxal and its oligomers	3.0 (s); 3.2 (m); 1.8 (s); 1.4 (s); 1.2 (s)	See Table S3b below <sup>6</sup>
Ethylene glycol	3.5 (s)	3.5 (s) <sup>7</sup>
Ethylene oxide	2.7 (s)	2.7 (s) (bought standard solution, see SI Fig. S6)



Table S3b. Predicted  $^1\text{H}$  NMR shifts for different methylglyoxal species<sup>6</sup>.

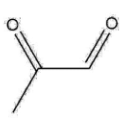
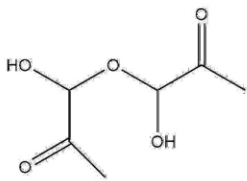
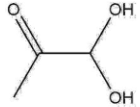
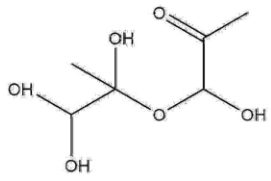
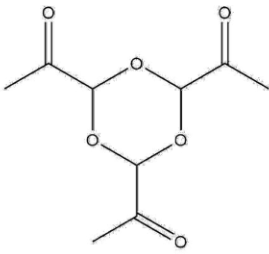
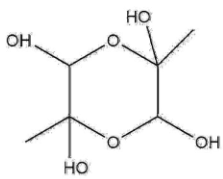
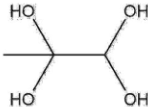
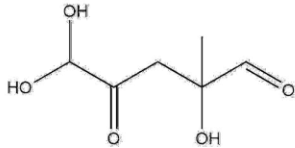
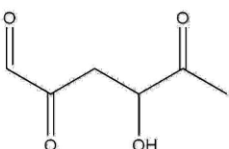
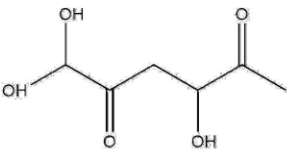
Compound	Predicted delta (ppm)	Compound	Predicted delta (ppm)
	2.067 (s) 9.560 (s)		2.095 (s) 5.726 (s)
	2.083 (s) 5.441 (s)		1.231 (s) 2.098 (s) 4.890 (s) 5.825 (s)
	2.100 (s) 5.378 (s)		1.301 (s) 4.415 (s)
	1.112 (s) 4.871 (s)		1.447 (s) 2.878 (s) 5.648 (s) 9.615 (s)
	2.069 (s) 3.148 (d) 4.66 (t) 9.597 (s)		2.069 (s) 3.07 (d) 4.658 (t) 5.645 (s)

Table S4: Boron NMR chemical shifts for boron species and references.

	$^{11}\text{B}$ Chemical Shift (ppm)	Reference (ppm)
$\text{H}_3\text{BO}_3$ Boric acid monomer	19	19 <sup>8,9</sup>
$(\text{B}_3\text{O}_3)\text{OH}_4^-$ Borate trimer	16	14 <sup>9</sup>
$(\text{OCH}_2\text{CH}_2\text{O})_2\text{B}$ Ethylene glycol borate diester	9	9 <sup>8</sup>

## 6. Liquid products analysis by high performance liquid chronoamperometry

The liquid products were detected and quantified by an offline high-performance liquid chromatography (HPLC; Perkin Elmers Flexer) with an autosampler, UV-vis detector and refractive index detector (RID). Separation was performed on a polymer-based matrix (polystyrene divinylbenzene) column (BioRad HPX 87H Aminex), with injection volumes of 10  $\mu\text{L}$ . The runtime was 60 minutes at a flow rate of 0.3  $\text{mL min}^{-1}$  and 45  $^{\circ}\text{C}$ . The calibration ( $R^2 > 0.99$ ) for furandiol, Product assignment was established by retention time and confirmed by  $^1\text{H NMR}$  (chemical shifts and splitting multiplicity), as described in detail in the ESI. All measurements were repeated three times on identically prepared and independent samples for statistical significance. For the analysis of all products including HCOOH, methylglyoxal, 2,3-furandiol and ethylene glycol, the HPLC spectra and standard curve is shown below.

$\mu\text{g/ml}$  in dicloromethane

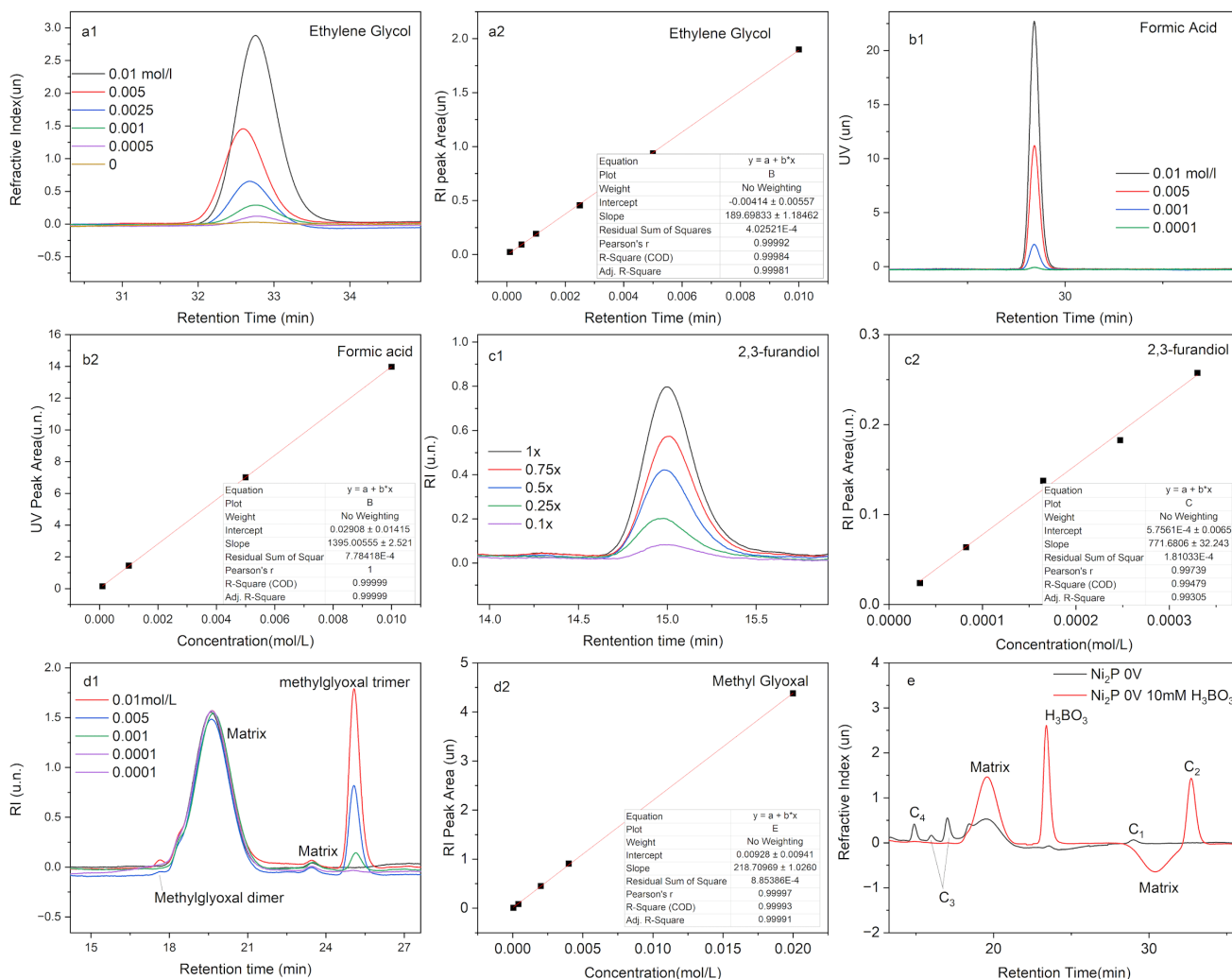


Fig. S5: (a) The spectra and calibration curve for ethylene glycol standards (a1, a2), formic acid standard (b1, b2), 2,3-furandiol (c1, c2), methylglyoxal (d1, d2); (e) The representative HPLC spectra for electrolyte of  $\text{CO}_2\text{RR}$  on  $\text{Ni}_2\text{P}$  with/without boric acid.

## 7. NMR and HPLC of the standards: Ethylene glycol, Ethylene oxide and DMSO

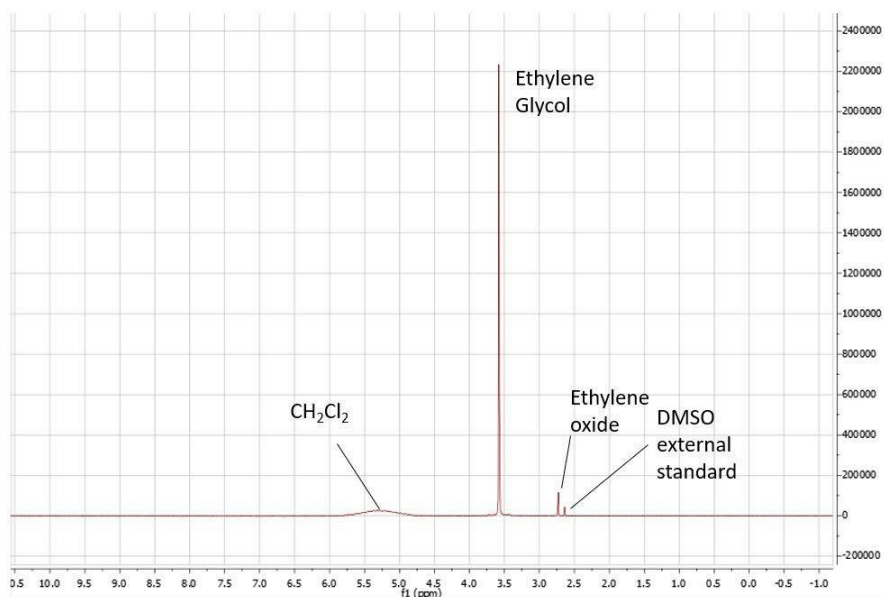


Fig. S6: The NMR spectra of the EO and DMSO standards. EO was purchased from Supelco (2000  $\mu\text{g/ml}$  in dichloromethane).

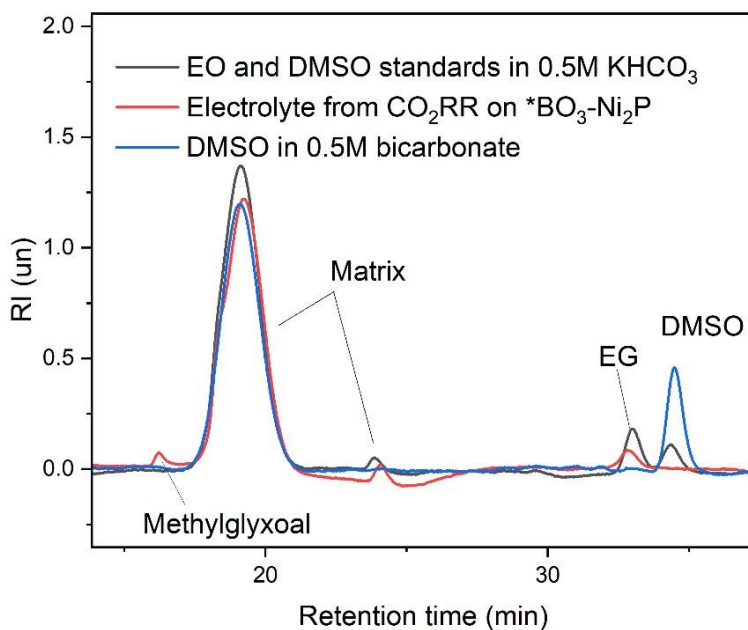


Fig. S7: The HPLC of the EO and DMSO standards (Supelco) in 0.5M KHCO<sub>3</sub> (black), DMSO in 0.5 M KHCO<sub>3</sub> (blue) and electrolyte from CO<sub>2</sub>RR on BO<sub>3</sub>\*-Ni<sub>2</sub>P in 0.5 M KHCO<sub>3</sub> at 0V vs RHE (red). Detection is done by refractive index (RI). The Matrix peaks refers to the electrolyte buffer. The ethylene oxide is hydrolyzed to ethylene glycol due to the acidic mobile phase: 5mM sulfuric acid aqueous solution.



## 9. Inductively Coupled Plasma Optical Emission Spectrometry (ICP-OES)

ICP-OES was conducted on a Perkin Elmer Optima 7300 DV to detect the amount of phosphorus and nickel that leached into the solution during the electrolysis. The samples were prepared by diluting 500  $\mu\text{L}$  of the post-reaction electrolyte with 2500  $\mu\text{L}$  of 5% (v/v) nitric acid in ultrapure water. The calibration curve for nickel and phosphorus were shown below prepared by SPEX Certiprep certified analytical standards.

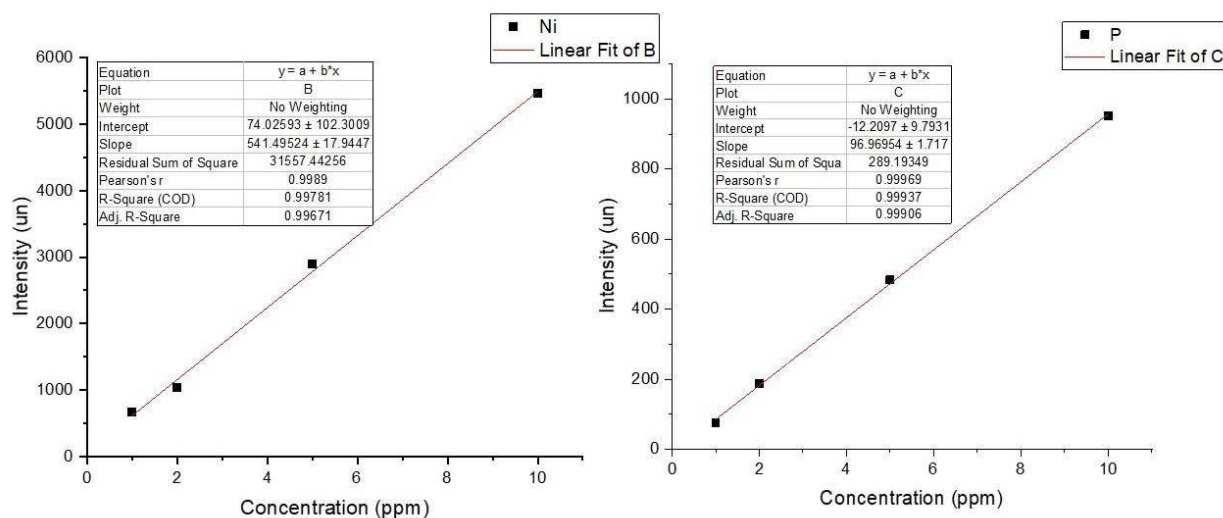


Fig. S8: The Calibration curves for nickel and phosphorous.

Table S6: The calculated nickel and phosphorous leaching in the electrolyte at the conditions tested  $\pm$  standard deviation between at least three chronoamperometry experiments.

	Ni	Standard Dev	P	Standard Dev
0mM $\text{H}_3\text{BO}_3$	0.015%	8.71392E-05	0.010%	1.92E-05
10mM $\text{H}_3\text{BO}_3$	0.016%	3.85051E-05	0.008%	1.55E-05
25mM $\text{H}_3\text{BO}_3$	0.023%	6.90082E-05	0.009%	1.76E-05
10mM $\text{H}_3\text{BO}_3$ - 100mV	0.013%	4.67512E-05	0.007%	4.68E-05
10mM $\text{H}_3\text{BO}_3$ - 200mV	0.013%	7.27262E-05	0.006%	2.14E-05

## 10. Control Experiments

To determine the organic products detected during the experiments originated from the CO<sub>2</sub> instead of the degradation of the membrane or the ionomer used in the electrode preparation, control experiments are conducted. The control experiment is conducted with Argon purged 0.25 M pyrophosphate buffer with 10 mM H<sub>3</sub>BO<sub>3</sub> on a typical Ni<sub>2</sub>P pellet electrode. Electrolysis was performed at 0.0 V vs RHE for 16h to determine if any products could have resulted from reductive degradation of the cell, membrane, or ionomer. No organic compounds were detected by NMR or HPLC as shown below.

Our choice of Na<sub>4</sub>P<sub>2</sub>O<sub>7</sub> electrolyte for the control experiments was guided by two factors. Our prior experience and the literature<sup>6</sup> have shown that under the condition of Ar purging using KHCO<sub>3</sub> electrolyte on nickel phosphides, CO<sub>2</sub>RR is still inevitable, considering the equilibrium between HCO<sub>3</sub><sup>-</sup> and CO<sub>2</sub> in aqueous solution. Therefore, KHCO<sub>3</sub> cannot be used for the LSV to measure HER.

Most literature reports use N<sub>2</sub> or Ar purging of 0.5 M phosphate buffer to conduct the LSV testing for HER. We used 0.25 M pyrophosphate buffer which has the same ionic strength as 0.5 M phosphate buffer. The pH of the 0.25 M pyrophosphate buffer was adjusted to 7.5 to match the CO<sub>2</sub> purged 0.5 M KHCO<sub>3</sub> buffer (7.5), and lower than the pH of the 0.5 M KHCO<sub>3</sub> buffer without CO<sub>2</sub> purging (8.4). Another reason why we did not choose phosphate buffer is due to interference in HPLC. Phosphate has an elution peak that overlaps with methylglyoxal in HPLC.

The choice of alkali metal counter cation can affect the distribution of CO<sub>2</sub>RR products, as seen on copper catalyst at high negative bias where ion adsorption/pairing on the surface can occur and influence the product distribution. The difference is minor for Na<sup>+</sup> vs K<sup>+</sup> and disappears at low electrical bias as used in our studies. Moreover, the cation effect cannot influence the product distribution of the CO<sub>2</sub>RR since K<sup>+</sup> is the only cation used for all CO<sub>2</sub>RR experiments.

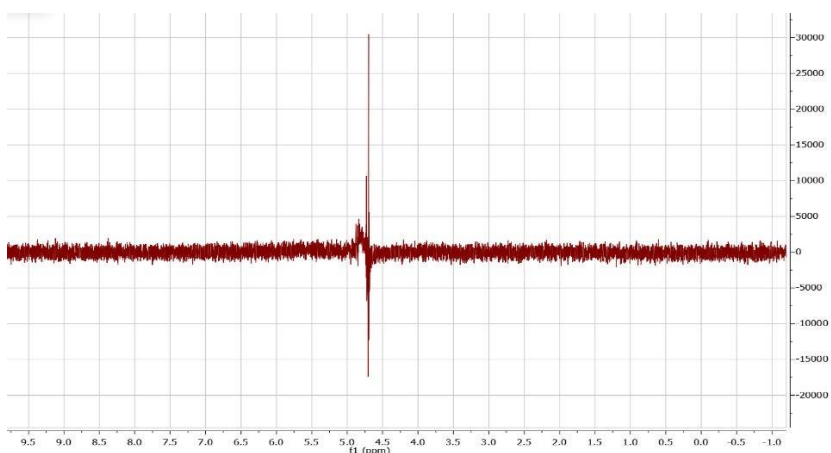


*Fig. S9: NMR of the electrolyte after 6h electrolysis on Ni<sub>2</sub>P at 0V vs RHE in Argon purged 0.25M sodium pyrophosphate and 10mM boric acid. Only water suppression peak at 4.7ppm appears.*

## 11. B1s/ P2s XPS for $\text{BO}_3^*-\text{Ni}_2\text{P}$

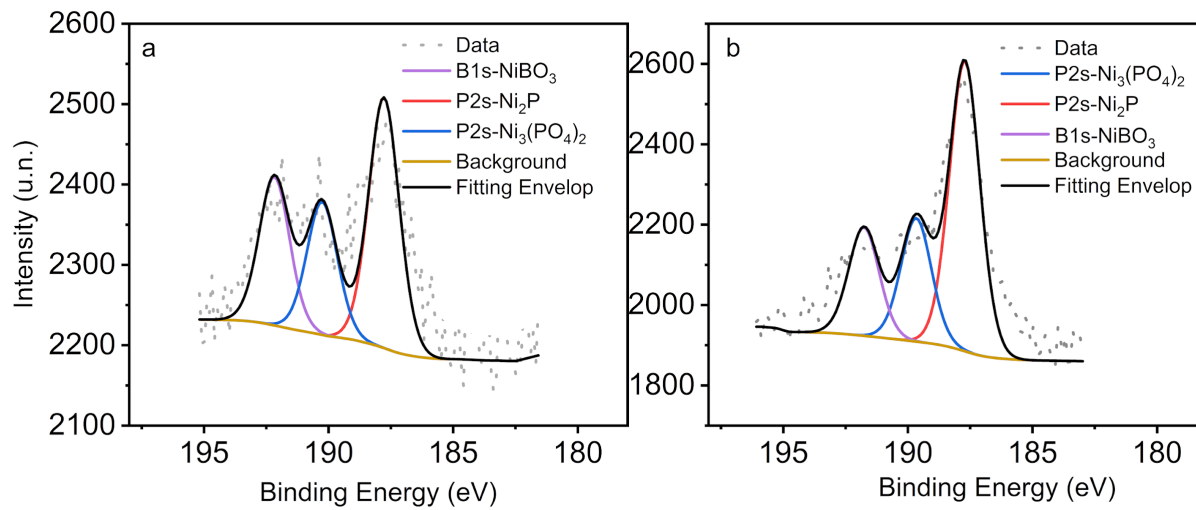


Fig. S10: B1s/P2s XPS spectra for  $\text{BO}_3^*-\text{Ni}_2\text{P}$  treated by 100 mM  $\text{H}_3\text{BO}_3$  (a) and 200 mM  $\text{H}_3\text{BO}_3$  (b).

## 12. High resolution TEM imaging and FFT analysis

TEM observation was conducted in a Talos F200X TEM under high vacuum operating at 200 kV electron accelerating voltage using a combination of bright-field (BF) TEM imaging and HRTEM imaging.

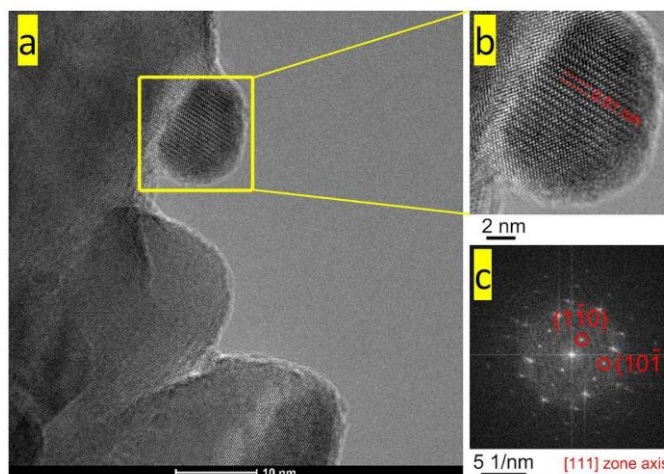


Fig S11: (a) High-resolution transmission electron microscopy (HRTEM) image of the Ni<sub>2</sub>P microparticle. (b) Zoomed-in HRTEM image of the region boxed by yellow lines in (a). (c) Fast Fourier transformation analysis of the whole HRTEM image in (b), showing a FFT pattern along the [111] zone axis.

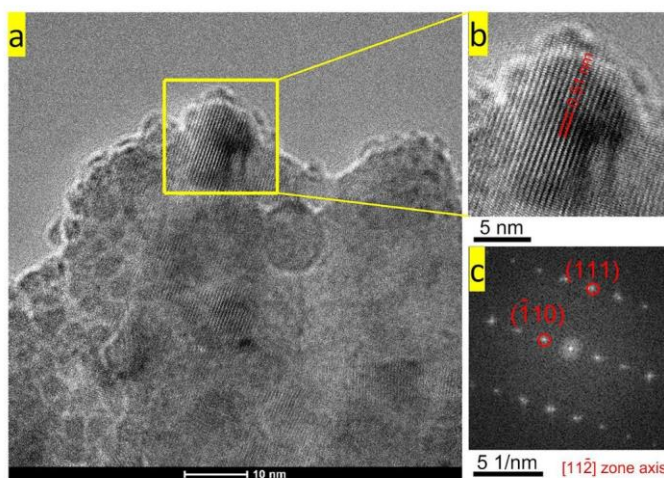


Fig S12: (a) High-resolution transmission electron microscopy (HRTEM) image of the Ni<sub>2</sub>P microparticle. (b) Zoomed-in HRTEM image of the region boxed by yellow lines in (a). (c) Fast Fourier transformation analysis of the whole HRTEM image in (b), showing a FFT pattern along the [11-2] zone axis.



### 13. Stability Test

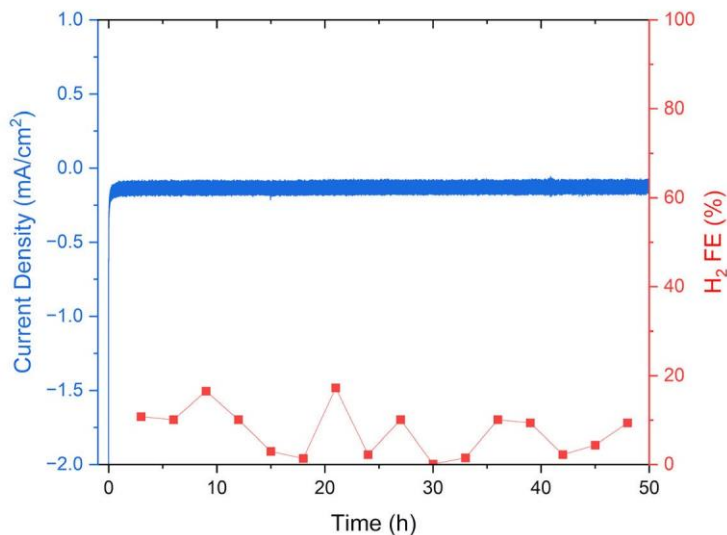


Fig S13: Total current density (blue) and H<sub>2</sub> Faradic Efficiency (red) obtained at time intervals during 50 hours of chronoamperometry on Ni<sub>2</sub>P in 0.5M KHCO<sub>3</sub> and 10 mM H<sub>3</sub>BO<sub>3</sub> in solution.

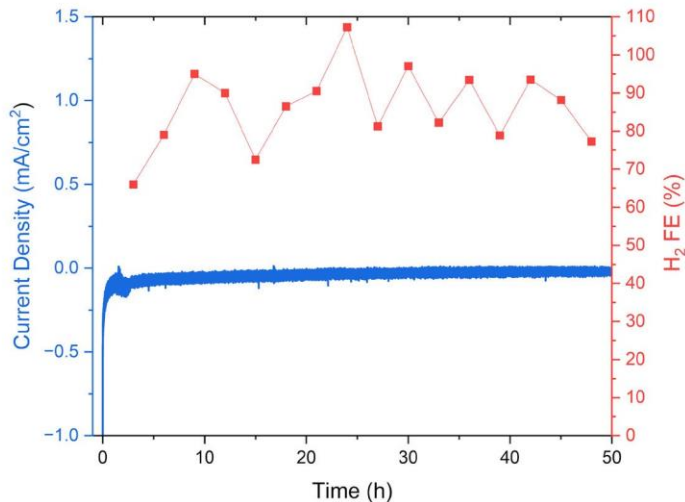


Fig S14: Total current density (blue) and H<sub>2</sub> Faradic Efficiency (red) obtained at time intervals during 50 hours of chronoamperometry for CO<sub>2</sub>RR on BO<sub>3</sub>\*-Ni<sub>2</sub>P in 0.5M KHCO<sub>3</sub> with no free boric acid in solution. The mean FE of H<sub>2</sub> products during the 50-h electrolysis is 86% and the remaining FE is due to CO<sub>2</sub>RR. Formation of the BO<sub>3</sub>\*-Ni<sub>2</sub>P catalyst was done prior to these measurements by electrolysis in 50 mM boric acid plus electrolyte for 6 h at 0 V applied potential.

## References

1. Hulbert, B. S.; Kriven, W. M., Erratum: Specimen-displacement correction for powder X-ray diffraction in Debye-Scherrer geometry with a flat area detector. Erratum. *J Appl Crystallogr* **2023**, *56* (Pt 2), 576.
2. NIST X-ray Photoelectron Spectroscopy (XPS) Database. [https://srdata.nist.gov/xps/main\\_search\\_menu.aspx](https://srdata.nist.gov/xps/main_search_menu.aspx) (accessed March 2nd).
3. Fa, D.; Yu, B.; Miao, Y., Synthesis of ultra-long nanowires of nickel phosphate by a template-free hydrothermal method for electrocatalytic oxidation of glucose. *Colloids and Surfaces A: Physicochemical and Engineering Aspects* **2019**, *564*, 31-38.
4. Mirghni, A. A.; Madito, M. J.; Oyedotun, K. O.; Masikhwa, T. M.; Ndiaye, N. M.; Ray, S. J.; Manyala, N., A high energy density asymmetric supercapacitor utilizing a nickel phosphate/graphene foam composite as the cathode and carbonized iron cations adsorbed onto polyaniline as the anode. *RSC Adv* **2018**, *8* (21), 11608-11621.
5. Elsener, B.; Atzei, D.; Krolikowski, A.; Rossi, A., Effect of phosphorus concentration on the electronic structure of nanocrystalline electrodeposited Ni-P alloys: an XPS and XAES investigation. *Surface and Interface Analysis* **2008**, *40* (5), 919-926.
6. Calvino, K. U. D.; Laursen, A. B.; Yap, K. M. K.; Goetjen, T. A.; Hwang, S.; Murali, N.; Mejia-Sosa, B.; Lubarski, A.; Teeluck, K. M.; Hall, E. S.; Garfunkel, E.; Greenblatt, M.; Dismukes, G. C., Selective CO<sub>2</sub> reduction to C<sub>3</sub> and C<sub>4</sub> oxyhydrocarbons on nickel phosphides at overpotentials as low as 10 mV. *Energy & Environmental Science* **2018**, *11* (9), 2550-2559.
7. Calvino, K. U. D.; Alherz, A. W.; Yap, K. M. K.; Laursen, A. B.; Hwang, S.; Bare, Z. J. L.; Clifford, Z.; Musgrave, C. B.; Dismukes, G. C., Surface Hydrides on Fe<sub>2</sub>P Electrocatalyst Reduce CO<sub>2</sub> at Low Overpotential: Steering Selectivity to Ethylene Glycol. *J Am Chem Soc* **2021**, *143* (50), 21275-21285.
8. Bishop, M.; Shahid, N.; Yang, J.; Barron, A. R., Determination of the mode and efficacy of the cross-linking of guar by borate using MAS 11B NMR of borate cross-linked guar in combination with solution 11B NMR of model systems. *Dalton Trans* **2004**, (17), 2621-34.
9. Fletcher, C.; Jiang, Y.; Amal, R., Production of formic acid from CO<sub>2</sub> reduction by means of potassium borohydride at ambient conditions. *Chemical Engineering Science* **2015**, *137*, 301-307.